Editors' Suggestion

Properties of Donor Qubits in ZnO Formed by Indium-Ion Implantation

Xingyi Wang,[1,*,†] Christian Zimmermann,[2,†] Michael Titze,[3] Vasileios Niaouris,[2] Ethan R. Hansen,[2] Samuel H. D'Ambrosia,[2] Lasse Vines,[4] Edward S. Bielejec,[3] and Kai-Mei C. Fu[1,2,5]

[1] *Department of Electrical Engineering, University of Washington, Seattle, Washington 98195, USA*
[2] *Department of Physics, University of Washington, Seattle, Washington 98195, USA*
[3] *Sandia National Laboratories, Albuquerque, New Mexico 87123, United States*
[4] *Department of Physics and Centre for Materials Science and Nanotechnology, University of Oslo, Blindern, N-0316 Oslo, Norway*
[5] *Physical Sciences Division, Pacific Northwest National Laboratory, Richland, Washington 99352, USA*

(Received 13 December 2022; revised 12 January 2023; accepted 17 April 2023; published 30 May 2023; corrected 13 November 2023)

Neutral shallow donors (D^0) in ZnO have emerged as a promising candidate for solid-state spin qubits. Here we report on the formation of D^0 in ZnO via implantation of In and subsequent annealing. The implanted In donors exhibit optical and spin properties on par with those of *in situ*–doped donors. The inhomogeneous linewidth of the donor-bound-exciton transition is less than 10 GHz, comparable to the optical linewidth of *in situ* In. Longitudinal spin relaxation times (T_1) exceed reported values for *in situ* Ga donors, indicating that residual In-implantation damage does not degrade T_1. Two-laser Raman spectroscopy of the donor spin reveals the hyperfine interaction of the donor electron with the spin-9/2 In nuclei. This work is an important step toward the deterministic formation of In-donor qubits in ZnO with optical access to a long-lived nuclear-spin memory.

DOI: 10.1103/PhysRevApplied.19.054090

I. INTRODUCTION

Neutral shallow donors (D^0) in semiconductors have shown potential as solid-state spin qubits for use in quantum technologies, such as quantum computing and quantum communication [1–4]. In direct-band-gap semiconductors, the bound electron spin states of shallow donors forming the qubit states can be optically accessed via the donor-bound exciton (D^0X) with high radiative efficiency [5,6]. The direct-band-gap semiconductor ZnO is an emerging platform for D^0 qubits, with D typically consisting of Al, Ga, or In substituted on a Zn site, denoted as Al_{Zn}, Ga_{Zn}, or In_{Zn}, respectively. For these donor qubits, narrow optical D^0X linewidths, efficient radiative transitions, optical state initialization, long longitudinal spin relaxation times ($T_1 > 400$ ms), and moderate coherence times ($T_2 \approx 50$ μs) have been demonstrated [7–9].

One feature of qubits based on impurities is that impurities can be incorporated by ion implantation and subsequent annealing [10–13]. With use of ion implantation, donor density and depth can be controlled. Thus, one can introduce either high densities of donors for quantum memory and transduction applications [14,15] or low densities of individually addressable donor qubits for quantum computing and networks [1,2,16]. Using focused-ion-beam technology, one can also control the lateral positioning of the donor impurities [17,18], enabling the deterministic placement of single donor qubits after fabrication of photonic devices [19]. Moreover, for single site defects, such as substitutional donors, near-deterministic incorporation is possible [13].

Here we report on the optical and spin properties of In^0_{Zn} in ZnO formed at a depth of 200 nm through ion implantation and subsequent annealing. We focus on In^0_{Zn} because of the following favorable features: large binding energy (approximately 63.2 meV [20]), strong hyperfine interaction with the In nucleus [21,22] for access to a nuclear-spin quantum memory [23], and the availability of ZnO substrates with low residual In doping. Ion implantation at relatively large fluences has been used to yield impurity-related shallow donors in ZnO [24–28]. Here we focus on low implantation fluences and the resulting donor properties relevant to quantum information applications. We demonstrate that implanted In^0_{Zn} exhibit D^0X inhomogeneous optical-transition linewidths of less than 10 GHz, comparable to the narrowest linewidths observed for ingrown In^0_{Zn}. The narrow linewidths owing to low strain

*xingyiw@uw.edu
†X. Wang and C. Zimmermann contributed equally to this work.

and small spectral diffusion from charge traps indicate low implantation damage, which is consistent with the reported resilience of ZnO to radiation damage [29,30]. Favorable spin properties are also demonstrated, with measured T_1 times in the hundreds of milliseconds, approximately 4 times longer than the T_1 times observed for ingrown Ga^0_{Zn} donors [7]. Further, two-laser Raman spectroscopy of implantation-doped In^0_{Zn} demonstrates that we can begin to resolve the large hyperfine interaction between the bound electron and the In nucleus, pointing to the potential for an optical interface with a long-lived nuclear-spin memory.

II. SAMPLE PREPARATION

A hydrothermally grown ZnO-single-crystal substrate (Tokyo Denpa, $5 \times 5 \times 0.3$ mm^3) with a surface orientation of (0001) is used as the implantation substrate [31] (see Appendix A). In the remainder of this article, the [0001] direction of the crystal is referred to as the $\vec{c}$ axis. Ion implantation is performed with the Sandia Ion Beam Laboratory 6 MV Tandem accelerator. In is extracted as a negative ion with use of a pressed cathode filled with In wire. The landing energy of In^+ ions is 800 keV, leading to an implant depth of approximately 200 nm determined by our simulating the implantation process using the Stopping and Range of Ions in Matter software suite [32] (Fig. 1). The ions are focused with a magnetic quadrupole lens, giving a beam spot of 780×870 μm^2. The spot size is measured with a luminescent phosphor and imaged with a homemade camera setup. The imaging setup uses a 10-mm hole in the center of its final imaging mirror, allowing concentric imaging of the beam. The focused ion beam allows us to vary the ion-implantation fluence within a single sample. The nominal implantation fluence ranges from 10^8 to 10^{15} ions/cm^2. Postimplantation annealing at 700 °C in oxygen for 1 h is used to recover implantation damage.

Secondary-ion mass spectrometry (SIMS) is performed to characterize the In-implantation profile and to determine the background concentrations of Al and Ga, prominent donors present in the substrate [20,33,34]. A Cameca IMS 7f secondary-ion mass spectrometer equipped with a 15-keV O_2 primary-ion-beam source is used to record the concentration-versus-depth profiles of In, Al, and Ga. Absolute concentrations of In are obtained by our measuring ion-implanted reference samples, ensuring less than ±10% error in accuracy. For depth calibration, the sputtered crater depths are determined with a Dektak 8 stylus profilometer and a constant erosion rate is assumed.

As shown in Fig. 1, the measured peak implantation depth is consistent with the depth from simulation. However, the measured implantation fluence ranges from 5 times to more than 10 times the nominal fluence. Moreover, a fluence of 10^{11} cm^{-2} is measured in a nominally unimplanted control region. The discrepancy in the nominal and measured implantation fluences is attributed to

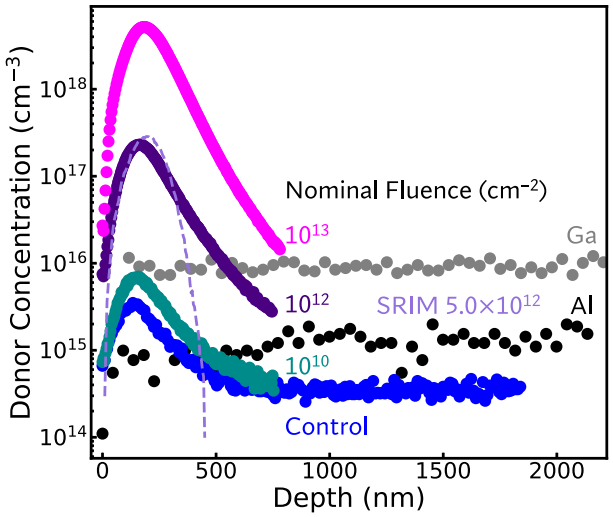

FIG. 1. SIMS data collected from the central 62 μm of a crater size of 200 μm. The measured (nominal) In-implantation fluences are 1.1×10^{14} cm^{-2} (10^{13} cm^{-2}), 5.0×10^{12} cm^{-2} (10^{12} cm^{-2}), 1.7×10^{11} cm^{-2} (10^{10} cm^{-2}), and 1.3×10^{11} cm^{-2} (control). The peak of In concentration from the SRIM simulated In-implantation profile matches well with that of the measured implantation profile.

overspray from the very-high-fluence implantation areas. Despite the higher-than-intended fluences, as we show below, the optical and spin properties of implanted In donors appear promising for quantum information applications. Throughout this work we refer to the implantation regions in terms of the nominal implantation fluence. Finally, a background concentration of 9.2×10^{15} cm^{-3} is measured for Ga and of 1.2×10^{15} cm^{-3} is measured for Al.

III. RESULTS AND DISCUSSION

The properties of the implanted In donors are characterized via low-temperature photoluminescence (PL) and PL-excitation (PLE) spectroscopy, spin-relaxation measurements, and two-laser coherent-population-trapping (CPT) measurements.

A. Photoluminescence Spectroscopy

The optical signature of donor incorporation in a semiconductor is the corresponding D^0X luminescence transition. Figure 2(a) shows a comparison of the normalized PL spectra from an as-grown ZnO single crystal and for a single crystal after In implantation and subsequent annealing. Before In implantation, a weak signal attributed to the $In^0_{Zn}X$ line [20] can be observed. The corresponding feature is about 3 orders of magnitude weaker than the PL features attributed to $Ga^0_{Zn}X$ and $Al^0_{Zn}X$ [20], indicating that In^0_{Zn} is present in concentrations on the order of 10^{13} cm^{-3}. After In implantation, a dramatic increase

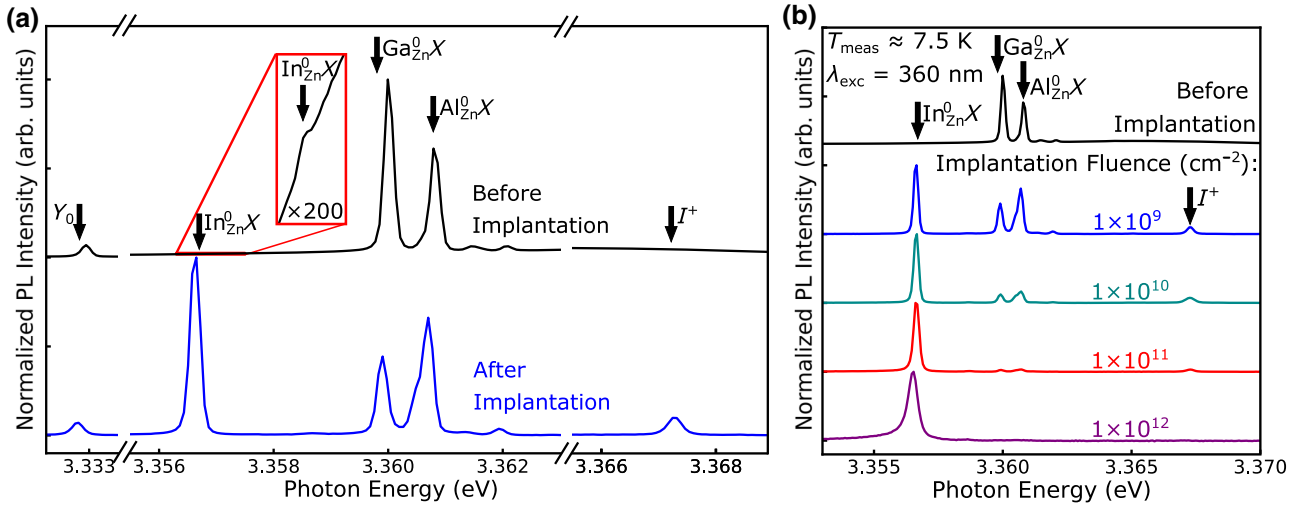

FIG. 2. (a) Comparison of normalized PL spectra of an as-grown ZnO single crystal and a single crystal after In implantation and subsequent annealing. (b) PL spectra normalized to the highest-intensity peak for different implantation fluences. $T = 7.5$ K, $\lambda_{exc} = 360$ nm, and $I_{exc} = 800$ nW/μm^2.

in the $In^0_{Zn}X$ line relative to the $Ga^0_{Zn}X$ and $Al^0_{Zn}X$ lines is observed. The $In^0_{Zn}X$ linewidth is spectrometer resolution limited up to a fluence of 10^{11} cm^{-2}. The complete fluence-dependent spectra are included in Appendix B.

In addition to the prominent $In^0_{Zn}X$ feature, a few additional new features can be observed after implantation and annealing. A sharp line at 3.3673 eV is labeled I^+ [see Fig. 2(a)]. This feature is close to a PL feature attributed to excitons bound to ionized In_{Zn} [35]. Magneto-PL measurements on this sample confirm that the I^+ line is related to an exciton bound to either an ionized donor or an ionized acceptor (see Appendix C), and we attribute the I^+ line to $In^+_{Zn}X$. Additionally, a low-energy shoulder on the $Al^0_{Zn}X$ line can be observed, indicating additional donor formation of unknown origin (see Appendix C). Finally, the prominent Y_0 exciton line, which is thought to arise from excitons bound to structural defects [20], can be seen in the sample both before and after In implantation.

Curiously, the absolute PL intensity of $In^0_{Zn}X$ remains approximately constant with implantation fluence [Fig. 3(a)], whereas the PL intensity of $Al^0_{Zn}X$, $Ga^0_{Zn}X$, and Y_0 decreases with increasing In-implantation fluence. These observed changes in the integrated PL intensity indicate that the entire volume of material probed with near-band-gap excitation ($\lambda_{exc} = 360$ nm) is affected by the In implantation. This does not necessarily mean the probing depth is only the 200 nm depth of implanted In ions, because intrinsic defects created during implantation could diffuse deeper into the material during annealing [36–38].

While the absolute PL intensity of $In^0_{Zn}X$ remains constant, the ratio of the integrated PL intensity of $In^0_{Zn}X$ and $Ga^0_{Zn}X$, denoted as $R_{In\text{-}Ga}$, increases with fluence, as shown in Fig. 3(b). $R_{In\text{-}Ga}$ cannot be tracked for fluences higher than 10^{12} cm^{-2} because the $Ga^0_{Zn}X$ line cannot be resolved at such high fluences. The constant $In^0_{Zn}X$ PL intensity coupled with the increase in $R_{In\text{-}Ga}$ with fluence suggests an implantation-induced decrease in the bound-exciton excitation efficiency and/or a decrease in radiative efficiency for all donors in the excitation volume.

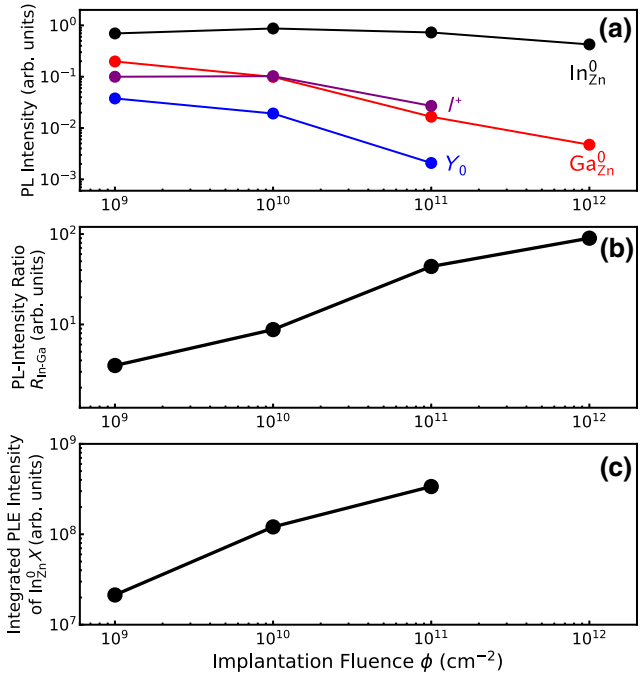

FIG. 3. (a) Dependence of PL intensity on In-implantation fluence for transitions labeled in Fig. 2(a). (b) Dependence of the ratio of the integrated PL intensity for $In^0_{Zn}X$ to $Ga^0_{Zn}X$, denoted $R_{In\text{-}Ga}$, on In-implantation fluence. (c) Integrated PLE intensity of $In^0_{Zn}X$. $T = 7.5$ K, $\lambda_{exc} = 360$ nm (for PL), and $I_{exc} = 800$ nW/μm^2.

Resonant-photoluminescence-excitation spectroscopy, described further below, supports the hypothesis that it is the off-resonant excitation efficiency and not the radiative efficiency that is primarily affected by implantation fluence.

B. Photoluminescence-Excitation Spectroscopy

In PLE spectroscopy, a narrowband laser scans the dominant transition, corresponding to relaxation from $In^0_{Zn}X$ to the $1s$ donor state of In^0_{Zn}, while two-electron satellites [TES; corresponding to relaxation to donor $2s/2p$ states, see the inset in Fig. 4(b)] and phonon-replica transitions are detected [9]. Resonant-excitation spectra of the two-electron satellites and phonon replicas are shown in Appendix E. Figure 4(a) shows the PLE spectra for an as-grown ZnO single crystal and for three different In-implantation fluences. The ability to perform resonant excitation of the $In^0_{Zn}X$ transition [see Fig. 2(b)] shows that an appreciable population of In_{Zn} exists in the desired neutral charge state.

Figure 4(b) displays the full width at half maximum (FWHM) extracted from PLE and PL spectra for all implantation fluences. For implantation fluences lower than 10^{10} cm^{-2}, the linewidth of implanted $In^0_{Zn}X$ is comparable to that of ingrown $In^0_{Zn}X$. For larger fluences, the linewidth of implanted $In^0_{Zn}X$ ensembles increases with increasing fluence, indicating that residual lattice damage contributes significantly to the inhomogeneous broadening. In contrast to PL measurements with 360-nm excitation, under resonant excitation we observe an increase in the $In^0_{Zn}X$ PLE intensity with implantation fluence [Fig. 3(c)]. This result indicates that the constant PL intensity with fluence observed in Fig. 3(a) is at least in part due to reduced excitation efficiency of D^0X. We also observe a linear relationship between PLE intensity and the PL ratio $R_{\text{In-Ga}}$ at low excitation fluence (see Appendix D). We thus use $R_{\text{In-Ga}}$ as a proxy for fluence in the tails of the implantation regions for finer fluence sampling [blue data in Fig. 4(b)].

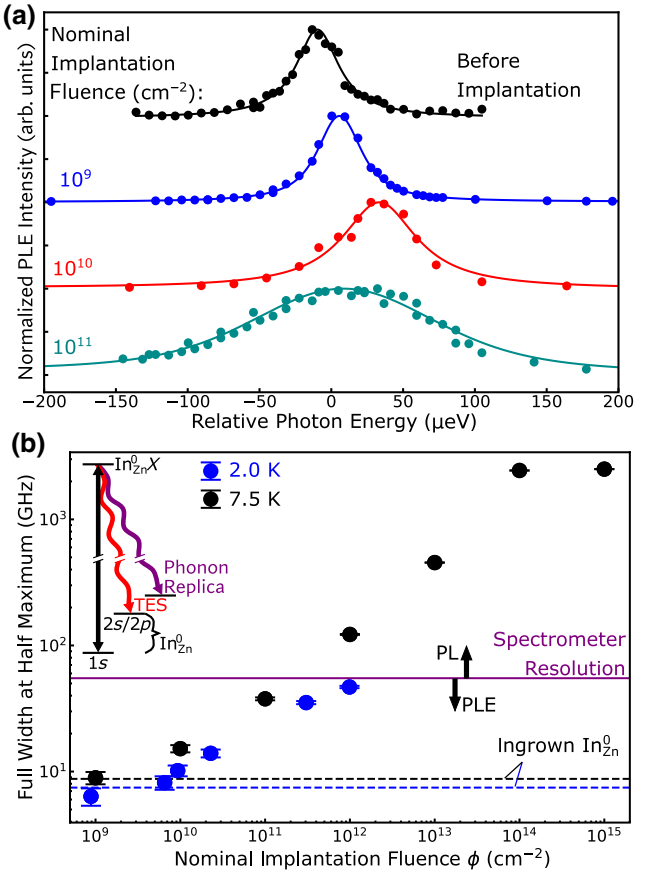

FIG. 4. (a) PLE spectra of $In^0_{Zn}X$ for ingrown and implanted In^0_{Zn}. The FWHM of each spectrum is determined by our fitting the spectrum to a Voigt profile. (b) Dependence of $In^0_{Zn}X$ FWHM on In-implantation fluence. The implantation fluence is estimated from $R_{\text{In-Ga}}$ for the data at 2.0 K (blue dots). Dashed lines indicate the FWHM of ingrown $In^0_{Zn}X$ at 2.0 and 7.5 K obtained for a ZnO single crystal with an In^0_{Zn} concentration similar to that of preimplanted sample.

C. Longitudinal Spin Relaxation

For ingrown Ga^0_{Zn}, we previously showed that the dominant mechanism for spin relaxation for the donor-bound spin-1/2 electron is due to spin-orbit coupling and the piezoelectric electron-phonon interaction [7]. Here we perform similar longitudinal-spin-relaxation measurements for implanted In^0_{Zn}. Figure 5 shows the dependence of T_1 on B in the Faraday geometry at 1.9 K for in-grown Ga^0_{Zn} and implanted In^0_{Zn}. The dependence of T_1 on B can be described by

$$T_1 = \left(\Gamma_{\downarrow\uparrow} + \Gamma_{\uparrow\downarrow}\right)^{-1} = \frac{1}{\Gamma_{\downarrow\uparrow}} \frac{\exp(\gamma) - 1}{\exp(\gamma) + 1},$$

with $\Gamma_{\downarrow\uparrow} = aB^5$, the relaxation rate from $|\uparrow\rangle$ to $|\downarrow\rangle$, and $\gamma = g_e \mu_B B / k_B T$ [7], where g_e is the electron g factor, μ_B is the Bohr magneton, and T is the temperature. The relaxation-rate prefactor a was found to be 0.08 s^{-1} T^{-5} as derived from the effective-mass theory [7]. For In^0_{Zn}, the same dependence on B is observed, however with an approximately-4-times-smaller prefactor a. This result indicates the longitudinal-spin-relaxation mechanism is identical for both types of donor, with no degradation observed for In due to residual implantation damage. The difference in the prefactor is expected from the dependence of both the spin-orbit interaction and piezo-phonon coupling on the effective-mass wave function. A small dependence of T_1 on implantation fluence is also observed (see Appendix F), which is consistent with the dependence of T_1 on donor density observed in Ga [7].

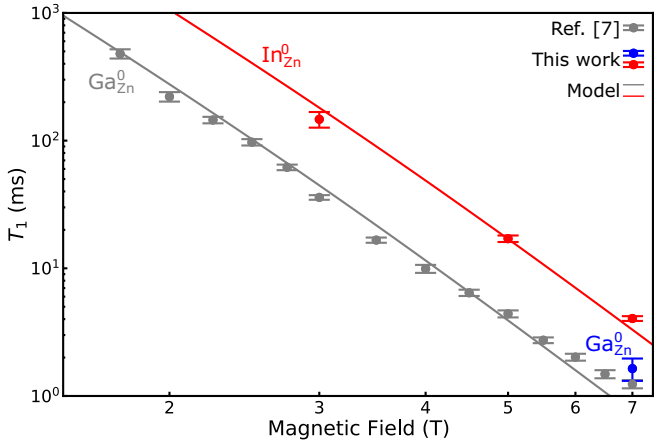

FIG. 5. Dependence of T_1 on the applied magnetic field. The population is optically initialized into the $|\uparrow\rangle$ state. Relaxation to the thermal equilibrium is probed optically (see Appendix F). Faraday geometry ($\vec{B} \parallel \vec{c}$), $T = 1.5$ K (for Ref. [7]), and $T = 1.9$ K (this work). Red, implanted In, fluence 10^9 cm^{-2}; blue, ingrown Ga; gray, ingrown Ga from a similar ZnO crystal, published in Ref. [7].

D. Two-Laser Spectroscopy and CPT

Two-laser spectroscopy can be further used to probe the spin properties of In^0_{Zn}. Figure 6(a) shows the results of resonant one-laser and two-laser spectroscopy performed at 7 T (Voigt geometry, $\vec{B} \perp \vec{c}$) and 2 K for a nominal implantation fluence of 10^9 cm^{-2}. The PL dependence on B and a discussion of the g factors can be found in Appendix G. When one laser (denoted as S) scans the $In^0_{Zn}X$-related transitions, four transitions can be resolved, corresponding to transitions between the two D^0 electron spin states and two D^0X hole spin states [Fig. 6(a)]. The overall PL intensity, however, is much lower than what is observed for measurements without a magnetic field. When a second laser (denoted as P) is resonant on the $|\downarrow\rangle$-to-$|\downarrow\uparrow\Uparrow\rangle$ transition, an enhancement in signal is seen when the scanning laser scans the transitions connected to $|\uparrow\rangle$. Without the pump laser (one-laser measurement), population is transferred from one spin state of the ground state to the other, where it is trapped and cannot be re-excited. When the second laser is placed resonantly on the opposite spin state, population is transferred back to the spin state that the scanning laser can excite.

The two-laser experiment performed here is often referred to as "reverse spectral hole burning" [39]. The observed antihole can be used to determine the homogeneous linewidth of an optical transition in the presence of inhomogeneous broadening; the pump laser repopulates only the subensemble resonant with the narrowband pump [39]. A double-Voigt fit to the antihole linewidth reveals a linewidth of 8 GHz at 2 K, surprisingly similar to the PLE linewidth at 0 T [see Fig. 4(a)]. For the reported lifetime of 1350 ps for $In^0_{Zn}X$ [20], the corresponding lifetime-limited linewidth is 120 MHz. Additionally, In^0_{Zn} exhibits a strong hyperfine interaction of the bound electron with the spin-9/2 In nucleus, which splits the electron spin into ten levels spaced by 50 MHz [21,22]. The expected linewidth of the reverse spectral hole is 550 MHz due to

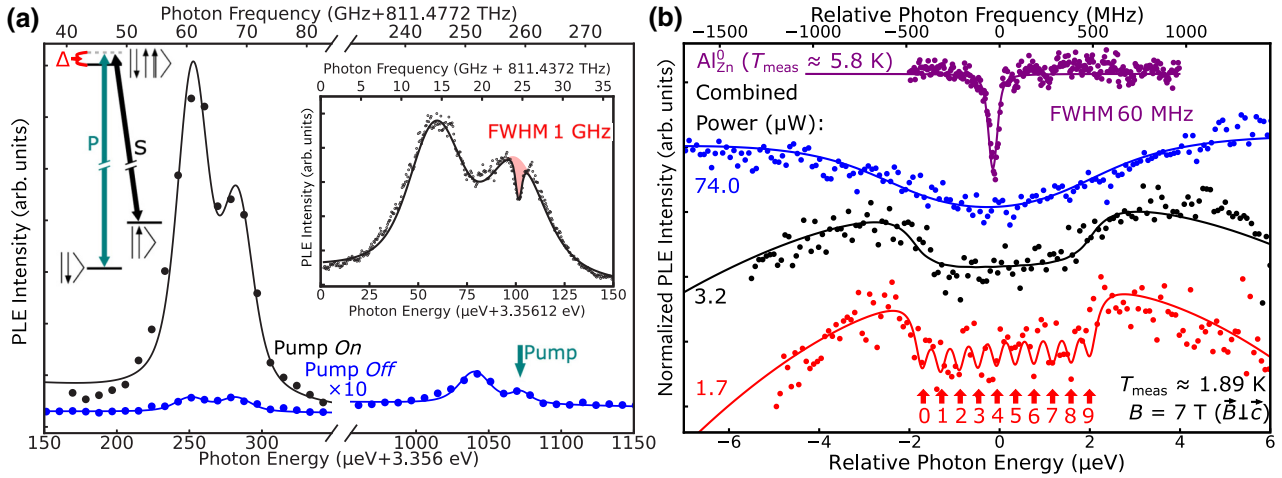

FIG. 6. (a) Resonant one-laser and two-laser spectroscopy performed on implanted (10^9 cm^{-2}) In^0_{Zn}. For the one-laser measurement (blue), a tunable laser scans all four transitions. For the two-laser measurement (see the inset on the left for the energy diagram, where the dashed gray level denotes the detuning of both lasers from the state $|\downarrow\uparrow\Uparrow\rangle$), the pump laser (P) is vertically polarized and resonant with the $|\downarrow\rangle$-to-$|\downarrow\uparrow\Uparrow\rangle$ transition, while the scanning laser (S) is horizontally polarized and tuned across the two transitions involving the $|\uparrow\rangle$ state. A high-resolution scan from the two-laser experiment is depicted in the right inset, in which a CPT dip is observed. (b) High-resolution PLE spectra showing CPT for different combined powers of the two lasers. For a constant wavelength of the pump laser, this leads to ten different resonance conditions depending on the nuclear spin m_I. The data are fitted to the sum of ten equally spaced Lorentzian profiles (splitting equal to $A \approx 100$ MHz). The full electron-nuclei energy diagram can be found in Appendix H. The measurements are performed at 7 T (Voigt geometry $\vec{B} \perp \vec{c}$) and 2 K.

the combined lifetime-limited linewidth and the hyperfine interaction. Thus, the 8-GHz antihole indicates additional broadening mechanisms that will be the subject of future investigations.

In addition to the antihole peak, a narrow 1-GHz dip can be observed on two-photon resonance [Fig. 6(a), inset]. The presence of the dip is the signature of coherent population trapping and the establishment of a ground-state spin coherence [9,40–43]. Figure 6(b) displays higher-resolution spectra for the CPT dip seen in Fig. 6(a) for different excitation powers for the scanning and pump lasers. Also included is a CPT spectrum for in-grown Al^0_{Zn} for reference. It is immediately evident that the CPT dip of In^0_{Zn} is much broader than the 60-MHz Al^0_{Zn} dip. Moreover, for lower combined powers of the scanning and pump lasers, the overall shape of the In CPT dip resembles an inverted top hat, rather than the Lorentzian or Gaussian line shape expected for a single homogeneously or inhomogeneously broadened transition. We attribute these unique features to the hyperfine interaction of the In-donor electron with the spin-9/2 In nucleus. At high fields, in which the electron spin number is a good quantum number, two-photon Raman transitions correspond to dips occurring between states of the same nuclear spin. Thus, ten dips separated by twice the hyperfine interaction are expected (see the energy diagram in Appendix H). For Al^0_{Zn}, one expects six dips separated by 1.5 MHz [44]. The In data shown in Fig. 6(b) are fit assuming ten Lorentzian dips spaced by 100 MHz. In the lowest-power In CPT spectrum, the best fit corresponds to a dip linewidth of 85 MHz; however, reasonable fits can be obtained for linewidths ranging from 50 to 170 MHz. Measurements of laser frequency drift and repeatability indicate the lack of resolved dips may be instrumentation limited at this time. However, the flat CPT bottom confirms the expected 100-MHz hyperfine interaction and a potential path toward optical nuclear-spin readout.

IV. CONCLUSION AND OUTLOOK

In summary, we demonstrate that ion implantation and annealing can be used to form In^0_{Zn} ensembles with promising optical and spin properties for quantum information applications. The implanted In^0_{Zn} exhibit optical linewidths of less than 10 GHz for the $In^0_{Zn}X$ transition, comparable with those of in-grown In^0_{Zn}. T_1 exceeds previously reported values for in-grown Ga^0_{Zn} [7], indicating that residual implantation damage has a negligible influence on longitudinal spin relaxation. Notably, the dominant longitudinal-spin-relaxation mechanism for In^0_{Zn} is the same process as was reported for Ga^0_{Zn} [7], but with a distinctively lower overall relaxation rate. Using two-laser resonant excitation, we demonstrate that a coherent superposition of the ground states of In^0_{Zn} can be created via CPT. Power-dependent CPT measurements indicate that, for low laser powers, the CPT line shape for In^0_{Zn} is determined by the hyperfine interaction between the donor-bound electron and the spin-9/2 In nucleus. Thus, it may be possible in the future to access the nuclear spin degrees of freedom of implanted In^0_{Zn} optically. These results demonstrate that ZnO is a promising host-material platform for low-damage creation of donor qubits via ion implantation and subsequent annealing, and thus the deterministic fabrication of donor spin qubits with optical access.

ACKNOWLEDGMENTS

The authors thank Yusuke Kozuka for the bulk ZnO substrates used for implantation, David Peterson for laser-marking the ZnO substrate, and Nicholas S. Yama for assistance in sample processing. This material is based on work primarily supported by the U.S. Department of Energy (DOE), Office of Science, Office of Basic Energy Sciences, under Award No. DE-SC0020378, and partially supported by Army Research Office MURI Grant on "Ab Initio Solid-State Quantum Materials: Design, Production and Characterization at the Atomic Scale" (Grant No. 18057522) and the National Science Foundation under Grant No. 2212017. This work was performed, in part, at the Center for Integrated Nanotechnologies, an Office of Science User Facility operated for the U.S. DOE, Office of Science. Sandia National Laboratories is a multimission laboratory managed and operated by National Technology and Engineering Solutions of Sandia, LLC, a wholly owned subsidiary of Honeywell International, Inc., for the U.S. DOE's National Nuclear Security Administration under Contract No. DE-NA-0003525. The views expressed in the article do not necessarily represent the views of the U.S. DOE or the U.S. Government.

APPENDIX A: SAMPLE LAYOUT

A grid pattern defining nine implantation areas is fabricated on the surface of the sample with a UV laser cutter (Protolaser U3) before implantation. Figure 7 shows the layout. Table I lists the nominal implantation fluences used for each region marked in Fig. 7.

APPENDIX B: PHOTOLUMINESCENCE SPECTRA WITH IMPLANTATION FLUENCE

Figure 8 shows normalized PL spectra for an as-grown ZnO single crystal and for different In-implantation regions after annealing. Each spectrum corresponds to a region in Fig. 7. The significant broadening of the $In^0_{Zn}X$ line at higher fluences is evident, and only the $In^0_{Zn}X$ transition can be observed for implantation fluences exceeding 10^{11} cm^{-2}.

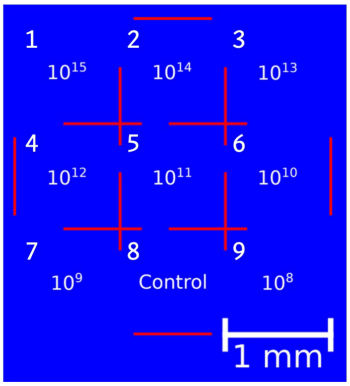

FIG. 7. Layout of the grid.

APPENDIX C: NEW DONOR LINES AFTER IMPLANTATION

Figure 9 shows PL intensity versus excitation power for an implantation fluence of 10^9 cm^{-2}. At powers above 9 μW, a low-energy shoulder on the Al peak (approximately 3.3606 eV) grows with increasing laser power. This shoulder is not observed in nonimplanted samples. The origin of this new excitonic feature is not known; however, it has energy similar to that of the I_7 line related to carbon impurities that was observed in prior work [45]. If this peak is carbon related, it is unclear how carbon was introduced during the In-implantation and annealing process.

The magneto-PL spectra at external magnetic fields in the Voigt geometry ($\vec{B} \perp \vec{c}$) from $B = 0$ T to $B = 7$ T in Fig. 10 show the Zeeman splittings of the transitions $In^0_{Zn}X$, $Ga^0_{Zn}X$, and $Al^0_{Zn}X$. In addition, the appearance of a transition at nonzero field near 3.3664 eV suggests a forbidden transition at zero field is allowed at nonzero field. Both this new transition at 3.3664 eV and the I^+ line at 3.3673 eV do not split at nonzero magnetic field. These observations are consistent with transitions that originate from excitons bound to ionized In donors $In^+_{Zn}X$ [46].

TABLE I. Summary of nominal implantation fluences and measured implantation fluences from SIMS for the different regions marked in Fig. 7.

Region	Nominal fluence (cm^{-2})	Measured fluence (cm^{-2})
1	10^{15}	Not measured
2	10^{14}	Not measured
3	10^{13}	1.1×10^{14}
4	10^{12}	5.0×10^{12}
5	10^{11}	Not measured
6	10^{10}	1.7×10^{11}
7	10^{9}	Not measured
8	0	1.3×10^{11}
9	10^{8}	Not measured

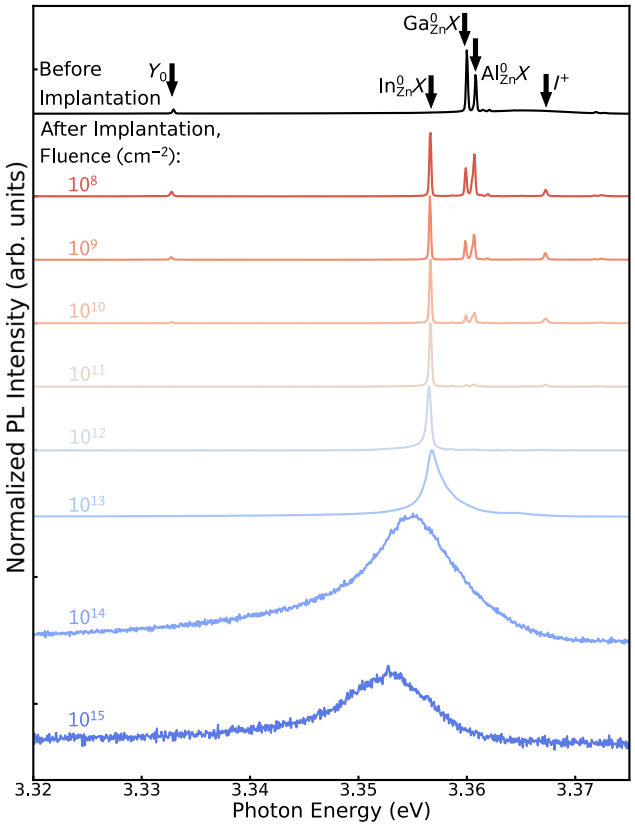

FIG. 8. PL spectra for an as-grown ZnO single crystal and for the crystal after In implantation of different fluences. The maximum intensity of each background-subtracted spectrum is normalized to unity. $T = 7.5$ K, $\lambda_{exc} = 360$ nm, and $I_{exc} = 800$ nW.

APPENDIX D: RELATIONSHIP BETWEEN INDIUM-GALLIUM PL RATIO AND PLE INTENSITY

We observe a linear relationship between the $In^0_{Zn}X$ PLE intensity A and the PL-intensity ratio $R_{In\text{-}Ga}$ for low

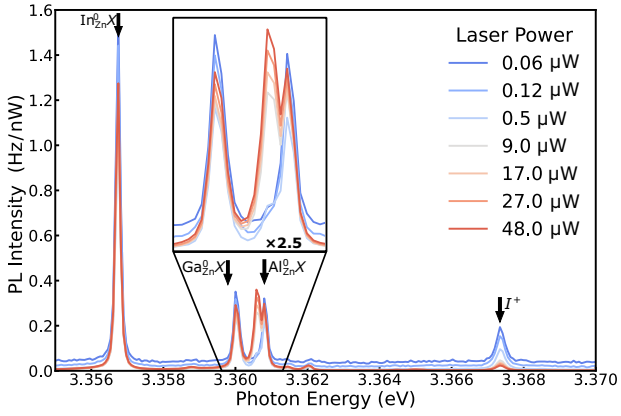

FIG. 9. PL intensity per laser power verses photon energy for 10^9-cm^{-2} implantation for different laser powers. $T = 10.5$ K and $\lambda_{exc} = 360$ nm.

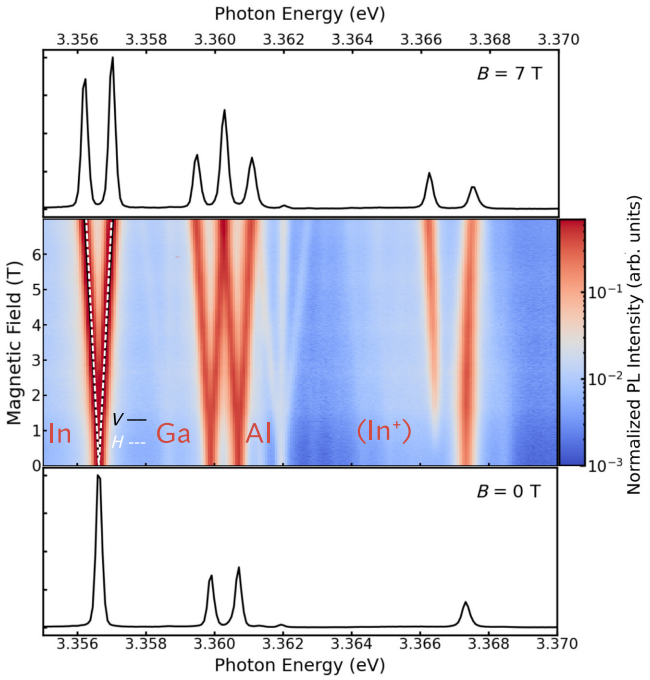

FIG. 10. The bottom panel shows the above-band PL spectrum of the In-implanted ZnO crystal, $B = 0$ T. The middle panel shows a heatmap of the above-band PL at $B = 0$–7 T. The dashed white line and the solid black line denote the transitions expected on the basis of the g factors of the electron and the hole determined in Appendix G. The top panel shows the above-band PL at $B = 7$ T. H, horizontal; V, vertical.

implantation fluences ($R_{\text{In-Ga}} < 30$). As shown in Fig. 11, by fitting a linear curve on 2-K and 7.5-K data, we estimate that $A = (0.23 \pm 0.01)R_{\text{In-Ga}}$ for $R_{\text{In-Ga}} < 30$. $R_{\text{In-Ga}} < 30$ corresponds to nominal implantation fluences lower than 5×10^{10} cm^{-2}.

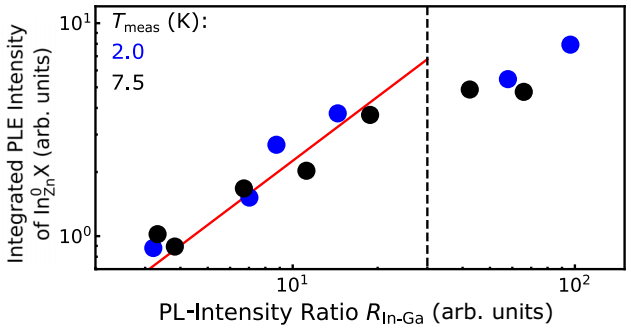

FIG. 11. PLE intensity of $\text{In}^0_{\text{Zn}}X$ as a function of the PL-intensity ratio between the $\text{In}^0_{\text{Zn}}X$ and $\text{Ga}^0_{\text{Zn}}X$ lines at 2 K (blue dots) and 7.5 K (black dots). The red line depicts a linearly fitted curve.

APPENDIX E: PHOTOLUMINESCENCE-EXCITATION SPECTROSCOPY

Figure 12(a) shows PLE spectra for implanted $\text{In}^0_{\text{Zn}}X$. The PLE intensity is plotted by our integrating the total signal of TES and phonon replicas. Figure 12(b) displays the corresponding spectra for the laser on resonance and off resonance with the $\text{In}^0_{\text{Zn}}X$ optical transition. The two-electron-satellite transitions can be observed only for neutral donors, and would not be observed for In^+_{Zn}.

APPENDIX F: LONGITUDINAL SPIN RELAXATION TIME

The longitudinal spin relaxation time T_1 of *in situ*–doped Ga^0_{Zn} donor ensembles was thoroughly investigated in Refs. [5,7]. T_1 is determined by measuring the

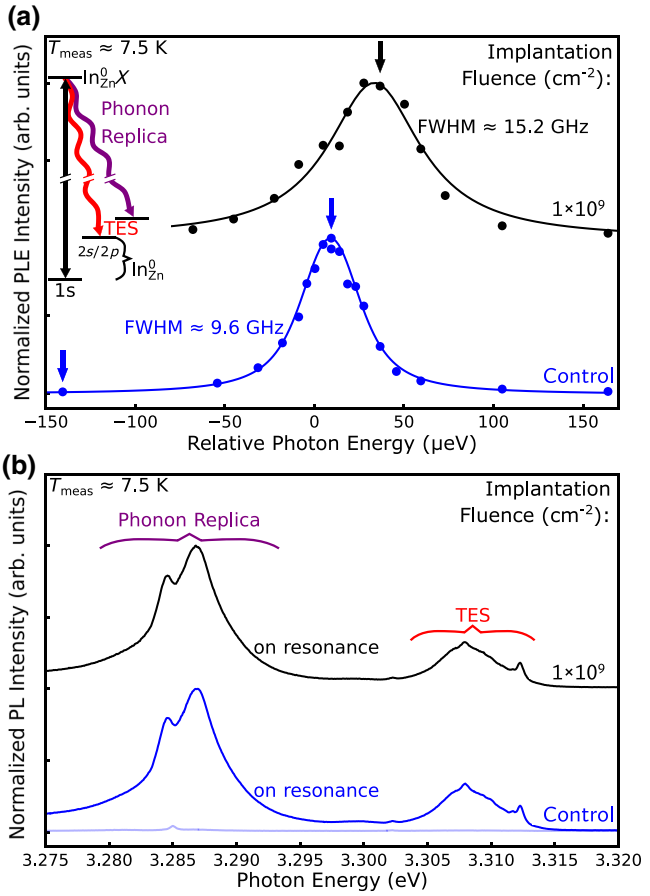

FIG. 12. (a) PLE spectra integrating the TES and phonon-replica signals (inset) for 10^9-cm^{-2} implantation and the control region. Full widths at half maximum of PLEs are obtained from fitted Voigt profiles. (b) Spectra of the TES and phonon replica on resonance and and off-resonance from $\text{In}^0_{\text{Zn}}X$ taken at excitation wavelengths marked by arrows in (a). The maximum intensity of each background-subtracted spectrum is normalized to unity. $T = 7.5$ K.

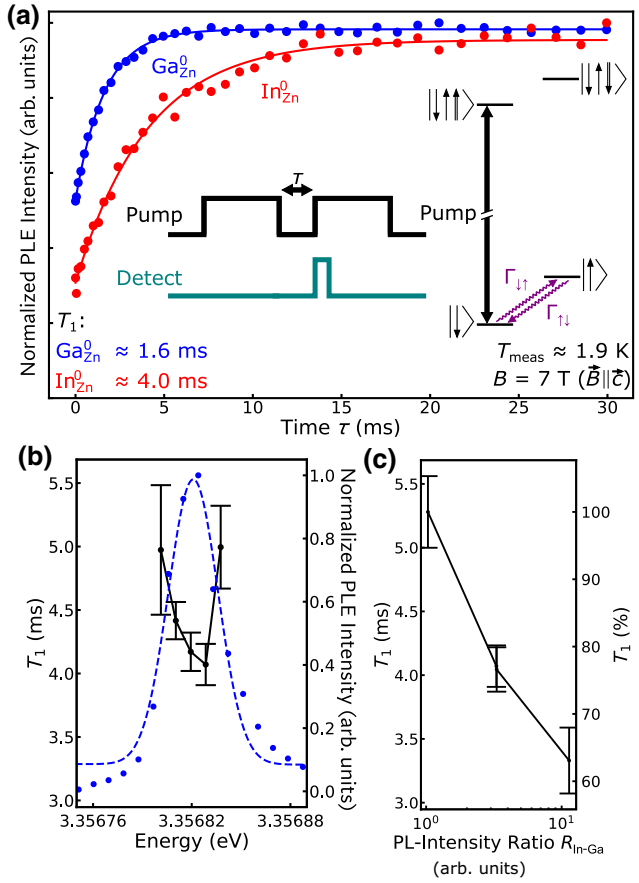

FIG. 13. (a) Population recovery of the state $|\downarrow\rangle$ from relaxation of the optically pumped state $|\uparrow\rangle$ as a function of delay time τ between each pump pulse for implanted In (10^9 cm^{-2}) and ingrown Ga. The insets show the pump and detect sequence and the energy-level diagram. T_1 is the decay constant of the fitted exponential profiles. (b) Longitudinal spin relaxation time T_1 of In^0_{Zn} as a function of excitation photon energy (black points, left y axis) and PLE spectrum (blue points, right y axis) for a fluence of 10^9 cm^{-2}. Pump pulse on resonance with $|\downarrow\rangle \Leftrightarrow |\downarrow\uparrow\Uparrow\rangle$. (c) T_1 as a function of the PL-intensity ratio between In^0_{Zn} and Ga^0_{Zn} denoted as $R_{In\text{-}Ga}$. Different ratios correspond to different implantation fluences (see the main text and Table I). Error bars are one standard deviation of the exponential fit of T_1 curves in (a). Faraday geometry ($\vec{B} \parallel \vec{c}$), $B = 7$ T, and $T = 1.9$ K.

population recovery of the spin state $|\downarrow\rangle$ after optical pumping of the population into the spin state $|\uparrow\rangle$ using resonant excitation for different delay times τ after the optical pumping pulse [see Fig. 13(a)]. The measurement scheme and energy-level diagram are shown as insets in Fig. 13(a).

In prior work [7], we demonstrated an excitation-energy dependence that was attributed to varying effective donor density at a given resonant (or near-resonant) excitation energy. In this work, we are able to directly investigate the donor density dependence of T_1 by probing locations of different implanted-In fluences. In Fig. 13(b), we show that for a given In fluence of 10^9 cm^{-2}, T_1 varies

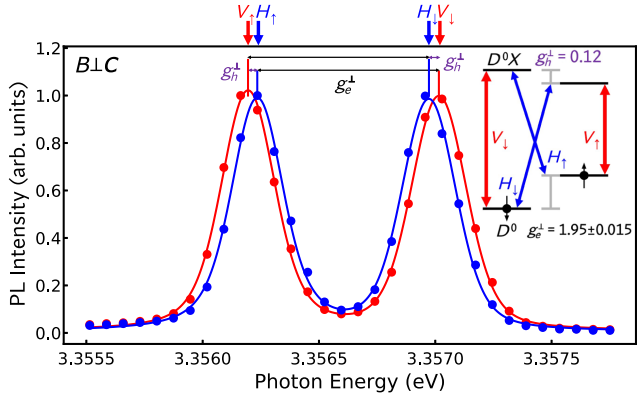

FIG. 14. Magneto-PL spectra taken with different polarization optics showing the energy separation used to find the g factors of the electron and the hole using $\Delta E = g\mu_B B$. The inset shows the energy-level diagram at $\vec{B} \perp \vec{c}$, $B > 0$. The measured lower bound of the hole g factor is 0.12 and the corresponding electron g, factor is 1.95.

with excitation energy, the same as what was observed from Ga donors in previous studies. A shorter longitudinal spin relaxation time is observed when probed on resonance with the ensemble implanted In donors, indicating that a higher density of probed subensemble shortens the measured longitudinal spin relaxation time. Figure 13(c) depicts the dependence of T_1 on the PL-intensity ratio between In^0_{Zn} and Ga^0_{Zn}, i.e., a proxy for implantation fluence. At higher implantation fluences, the longitudinal spin relaxation time becomes shorter, which agrees qualitatively with our explanation for the effective donor-density dependence of T_1.

APPENDIX G: g FACTORS OF NEUTRAL DONOR–BOUND EXCITONS

The D^0X Zeeman energy is determined by the unpaired hole spin. At nonzero external magnetic field perpendicular to the crystal axis (Voigt geometry $\vec{B} \perp \vec{c}$), the energy-level configuration of the four possible donor-bound-exciton transitions and each of their polarizations are labeled in the inset in Fig. 14. The splitting of the hole is small compared with that of the electron. At the experimentally applied fields, the separation between pairs of transitions $V_\downarrow$ and $H_\downarrow$ and $V_\uparrow$ and $H_\uparrow$ cannot be resolved. As shown in Fig. 14, by collecting vertical and horizontal polarizations, one can observe a shift in the excitonic emission. This shift represents a lower bound of the g factor of the hole, $g_h^\perp = 0.12$. The g factor of the electron is 1.95, which is in good agreement with Ref. [46].

APPENDIX H: COHERENT POPULATION TRAPPING

Figure 15 shows a schematic illustration of the two-photon transitions in the $In^0_{Zn}/In^0_{Zn}X$ system due to

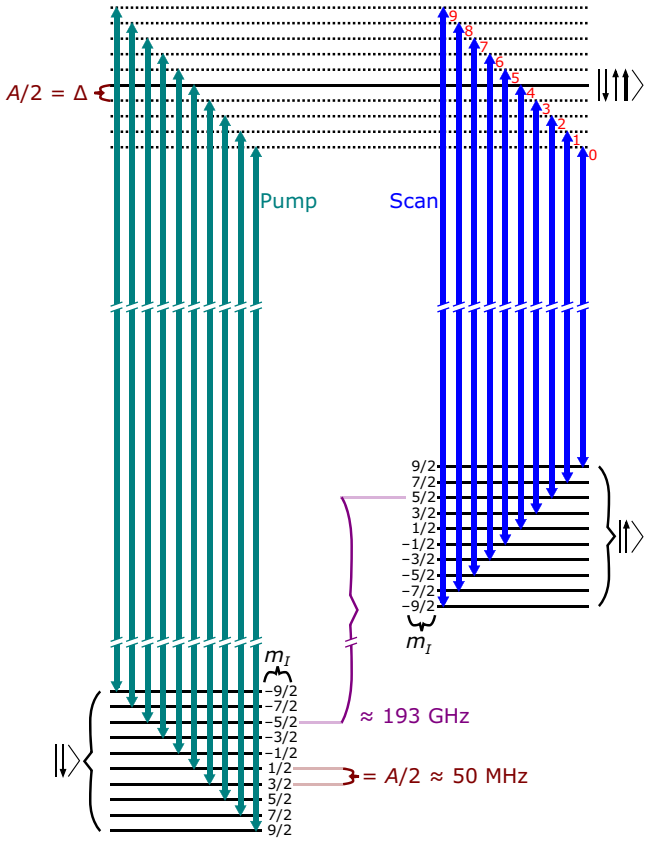

FIG. 15. Ten expected two-photon resonances of CPT due to the hyperfine interaction between the valence electron of In^0_{Zn} and In nuclei of the same m_I.

the hyperfine interaction between In nuclei (all stable In isotopes have $I = 9/2$) and the valence electron of In^0_{Zn} [21,22]. It is assumed that the two-photon resonance necessary for CPT can occur only between ground-state levels with the same nuclear spin quantum number (m_I), i.e., nuclear spin flips are forbidden. For a constant wavelength of the pump laser, this leads to different resonance conditions depending on m_I, i.e., different resonant wavelength for the scanning laser. We expect ten resonances equally spaced by A. CPT can occur at different detunings from the single level representing $|\downarrow\uparrow\Uparrow\rangle$. The hyperfine splitting of the excited state is expected to be much smaller than that of the ground state due to the spin-singlet nature of the electrons and the p-orbital nature of the hole.

[1] John J. L. Morton and Brendon W. Lovett, Hybrid solid-state qubits: The powerful role of electron spins, Annu. Rev. Condens. Matter Phys. **2**, 189 (2011).

[2] Y Yamamoto, T. D. Ladd, D Press, S Clark, K Sanaka, C Santori, D Fattal, K. M. Fu, S Höfling, S Reitzenstein, and A Forchel, Optically controlled semiconductor spin qubits for quantum information processing, Phys. Scr. **2009**, 014010 (2009).

[3] L. M. K. Vandersypen, H. Bluhm, J. S. Clarke, A. S. Dzurak, R. Ishihara, A. Morello, D. J. Reilly, L. R. Schreiber, and M. Veldhorst, Interfacing spin qubits in quantum dots and donors—hot, dense, and coherent, npj Quantum Inf. **3**, 34 (2017).

[4] Y. He, S. K. Gorman, D. Keith, L. Kranz, J. G. Keizer, and M. Y. Simmons, A two-qubit gate between phosphorus donor electrons in silicon, Nature **571**, 371 (2019).

[5] Xiayu Linpeng, Todd Karin, M. V. Durnev, Russell Barbour, M. M. Glazov, E. Ya. Sherman, S. P. Watkins, Satoru Seto, and Kai-Mei C. Fu, Longitudinal spin relaxation of donor-bound electrons in direct band-gap semiconductors, Phys. Rev. B **94**, 125401 (2016).

[6] Susan M. Clark, Kai-Mei C. Fu, Qiang Zhang, Thaddeus D. Ladd, Colin Stanley, and Yoshihisa Yamamoto, Ultrafast Optical Spin Echo for Electron Spins in Semiconductors, Phys. Rev. Lett. **102**, 247601 (2009).

[7] Vasileios Niaouris, Mikhail V. Durnev, Xiayu Linpeng, Maria L. K. Viitaniemi, Christian Zimmermann, Aswin Vishnuradhan, Yusuke Kozuka, Masashi Kawasaki, and Kai-Mei C. Fu, Ensemble spin relaxation of shallow donor qubits in ZnO, Phys. Rev. B **105**, 195202 (2022).

[8] Xiayu Linpeng, Maria L. K. Viitaniemi, Aswin Vishnuradhan, Y. Kozuka, Cameron Johnson, M. Kawasaki, and Kai-Mei C. Fu, Coherence Properties of Shallow Donor Qubits in ZnO, Phys. Rev. Appl. **10**, 064061 (2018).

[9] Maria L. K. Viitaniemi, Christian Zimmermann, Vasileios Niaouris, Samuel H. D'Ambrosia, Xingyi Wang, E. Senthil Kumar, Faezeh Mohammadbeigi, Simon P. Watkins, and Kai-Mei C. Fu, Coherent spin preparation of indium donor qubits in single ZnO nanowires, Nano Lett. **22**, 2134 (2022).

[10] Michael Titze, Heejun Byeon, Anthony Flores, Jacob Henshaw, C. Thomas Harris, Andrew M. Mounce, and Edward S. Bielejec, In situ ion counting for improved implanted ion error rate and silicon vacancy yield uncertainty, Nano Lett. **22**, 3212 (2022). pMID: 35426685,

[11] Srivatsa Chakravarthi, Chris Moore, April Opsvig, Christian Pederson, Emma Hunt, Andrew Ivanov, Ian Christen, Scott Dunham, and Kai-Mei C. Fu, Window into NV center kinetics via repeated annealing and spatial tracking of thousands of individual NV centers, Phys. Rev. Mater. **4**, 023402 (2020).

[12] J. C. McCallum, B. C. Johnson, and T. Botzem, Donor-based qubits for quantum computing in silicon, Appl. Phys. Rev. **8**, 031314 (2021).

[13] Alexander M. Jakob, Simon G. Robson, Vivien Schmitt, Vincent Mourik, Matthias Posselt, Daniel Spemann, Brett C. Johnson, Hannes R. Firgau, Edwin Mayes, Jeffrey C. McCallum, Andrea Morello, and David N. Jamieson, Deterministic single ion implantation with 99.87% confidence for scalable donor-qubit arrays in silicon, (2020),.

[14] Alexander I. Lvovsky, Barry C. Sanders, and Wolfgang Tittel, Optical quantum memory, Nat. Photon. **3**, 706 (2009).

[15] Lewis A. Williamson, Yu-Hui Chen, and Jevon J. Longdell, Magneto-optic Modulator with Unit Quantum Efficiency, Phys. Rev. Lett. **113**, 203601 (2014).

[16] Jennifer F. Lilieholm, Vasileios Niaouris, Alexander Kato, Kai-Mei C. Fu, and Boris B. Blinov, Photon-mediated

entanglement scheme between a ZnO semiconductor defect and a trapped Yb ion, Appl. Phys. Lett. **117**, 154002 (2020).

[17] J. L. Pacheco, M. Singh, D. L. Perry, J. R. Wendt, G. Ten Eyck, R. P. Manginell, T. Pluym, D. R. Luhman, M. P. Lilly, M. S. Carroll, and E. Bielejec, Ion implantation for deterministic single atom devices, Rev. Sci. Instrum. **88**, 123301 (2017).

[18] Syuto Tamura, Godai Koike, Akira Komatsubara, Tokuyuki Teraji, Shinobu Onoda, Liam P. McGuinness, Lachlan Rogers, Boris Naydenov, E. Wu, Liu Yan, Fedor Jelezko, Takeshi Ohshima, Junichi Isoya, Takahiro Shinada, and Takashi Tanii, Array of bright silicon-vacancy centers in diamond fabricated by low-energy focused ion beam implantation, Appl. Phys. Exp. **7**, 115201 (2014).

[19] Tim Schröder, Matthew E. Trusheim, Michael Walsh, Luozhou Li, Jiabao Zheng, Marco Schukraft, Alp Sipahigil, Ruffin E. Evans, Denis D. Sukachev, Christian T. Nguyen, Jose L. Pacheco, Ryan M. Camacho, Edward S. Bielejec, Mikhail D. Lukin, and Dirk Englund, Scalable focused ion beam creation of nearly lifetime-limited single quantum emitters in diamond nanostructures, Nat. Commun. **8**, 15376 (2017).

[20] M. R. Wagner, G. Callsen, J. S. Reparaz, J.-H. Schulze, R. Kirste, M. Cobet, I. A. Ostapenko, S. Rodt, C. Nenstiel, M. Kaiser, A. Hoffmann, A. V. Rodina, M. R. Phillips, S. Lautenschläger, S. Eisermann, and B. K. Meyer, Bound excitons in ZnO: Structural defect complexes versus shallow impurity centers, Phys. Rev. B **84**, 035313 (2011).

[21] D. Block, A. Hervé, and R. T. Cox, Optically detected magnetic resonance and optically detected ENDOR of shallow indium donors in ZnO, Phys. Rev. B **25**, 6049 (1982).

[22] C. Gonzalez, D. Block, R. T. Cox, and A. Herve, Magnetic resonance studies of shallow donors in zinc oxide, J. Cryst. Growth **59**, 357 (1982).

[23] John J. L. Morton, Alexei M. Tyryshkin, Richard M. Brown, Shyam Shankar, Brendon W. Lovett, Arzhang Ardavan, Thomas Schenkel, Eugene E. Haller, Joel W. Ager, and S. A. Lyon, Solid-state quantum memory using the ^{31}P nuclear spin, Nature **455**, 1085 (2008).

[24] T. E. Mølholt, H. P. Gunnlaugsson, K. Johnston, R. Mantovan, J. Röder, V. Adoons, A. Mokhles Gerami, H. Masenda, Y. A. Matveyev, M. Ncube, I. Unzueta, K. Bharuth-Ram, H. P. Gislason, P. Krastev, G. Langouche, D. Naidoo, S. Ólafsson, A. Zenkevich, and ISOLDE Collaboration, Charge states and lattice sites of dilute implanted Sn in ZnO, J. Phys.: Condens. Matter **29**, 155701 (2017).

[25] J. Cullen, D. Byrne, K. Johnston, E. McGlynn, and M. O. Henry, Chemical identification of luminescence due to Sn and Sb in ZnO, Appl. Phys. Lett. **102**, 192110 (2013).

[26] J. Cullen, K. Johnston, M. O. Henry, and E. McGlynn, Photoluminescence due to group IV impurities in ZnO, MRS Online Proc. Libr. **1394**, 1 (2012).

[27] S. Müller, D. Stichtenoth, M. Uhrmacher, H. Hofsäss, C. Ronning, and J. Röder, Unambiguous identification of the PL-I9 line in zinc oxide, Appl. Phys. Lett. **90**, 012107 (2007).

[28] D. A. Zatsepin, D. W. Boukhvalov, E. Z. Kurmaev, I. S. Zhidkov, S. S. Kim, L. Cui, N. V. Gavrilov, and S. O. Cholakh, XPS and DFT study of Sn incorporation into ZnO and TiO2 host matrices by pulsed ion implantation, Phys. Status Solidi (b) **252**, 1890 (2015).

[29] S. O. Kucheyev, P. N. K. Deenapanray, C. Jagadish, J. S. Williams, Mitsuaki Yano, Kazuto Koike, Shigehiko Sasa, Masataka Inoue, and Ken-ichi Ogata, Electrical isolation of ZnO by ion bombardment, Appl. Phys. Lett. **81**, 3350 (2002).

[30] S. O. Kucheyev, J. S. Williams, C. Jagadish, J. Zou, Cheryl Evans, A. J. Nelson, and A. V. Hamza, Ion-beam-produced structural defects in ZnO, Phys. Rev. B **67**, 094115 (2003).

[31] Katsumi Maeda, Mitsuru Sato, Ikuo Niikura, and Tsuguo Fukuda, Growth of 2 inch ZnO bulk single crystal by the hydrothermal method, Semicond. Sci. Technol. **20**, S49 (2005).

[32] James F. Ziegler, M. D. Ziegler, and J. P. Biersack, SRIM – the stopping and range of ions in matter (2010), Nucl. Instrum. Methods Phys. Res. Sect. B: Beam Interact. Mater. At. **268**, 1818 (2010). 19th International Conference on Ion Beam Analysis,

[33] L. Vines, E. V. Monakhov, R. Schifano, W. Mtangi, F. D. Auret, and B. G. Svensson, Lithium and electrical properties of ZnO, J. Appl. Phys. **107**, 103707 (2010).

[34] B. K. Meyer, H. Alves, D. M. Hofmann, W. Kriegseis, D. Forster, F. Bertram, J. Christen, A. Hoffmann, M. Straßburg, M. Dworzak, U. Haboeck, and A. V. Rodina, Bound exciton and donor–acceptor pair recombinations in ZnO, Phys. Status Solidi (b) **241**, 231 (2004).

[35] E. Senthil Kumar, F. Mohammadbeigi, L. A. Boatner, and S. P. Watkins, High-resolution photoluminescence spectroscopy of Sn-doped ZnO single crystals, J. Lumin. **176**, 47 (2016).

[36] Alexander Azarov, Vishnukanthan Venkatachalapathy, Zengxia Mei, Lishu Liu, Xiaolong Du, Augustinas Galeckas, Edouard Monakhov, Bengt G. Svensson, and Andrej Kuznetsov, Self-diffusion measurements in isotopic heterostructures of undoped and in situ doped ZnO: Zinc vacancy energetics, Phys. Rev. B **94**, 195208 (2016).

[37] T. N. Sky, K. M. Johansen, Y. K. Frodason, T Aarholt, H. N. Riise, Ø. Prytz, B. G. Svensson, and L. Vines, Diffusion of indium in single crystal zinc oxide: A comparison between group III donors, Semicond. Sci. Technol. **34**, 025011 (2019).

[38] Daniel Steiauf, John L. Lyons, Anderson Janotti, and Chris G. Van de Walle, First-principles study of vacancy-assisted impurity diffusion in ZnO, APL Mater. **2**, 096101 (2014).

[39] A. Yang, M. Steger, T. Sekiguchi, M. L. W. Thewalt, J. W. Ager, and E. E. Haller, Homogeneous linewidth of the ^{31}P bound exciton transition in silicon, Appl. Phys. Lett. **95**, 122113 (2009).

[40] Kai-Mei C. Fu, Charles Santori, Colin Stanley, M. C. Holland, and Yoshihisa Yamamoto, Coherent Population Trapping of Electron Spins in a High-Purity *n*-Type GaAs Semiconductor, Phys. Rev. Lett. **95**, 187405 (2005).

[41] Charles Santori, Philippe Tamarat, Philipp Neumann, Jörg Wrachtrup, David Fattal, Raymond G. Beausoleil, James Rabeau, Paolo Olivero, Andrew D. Greentree, Steven Prawer, Fedor Jelezko, and Philip Hemmer, Coherent Population Trapping of Single Spins in Diamond under Optical Excitation, Phys. Rev. Lett. **97**, 247401 (2006).

[42] H. R. Gray, R. M. Whitley, and C. R. Stroud, Coherent trapping of atomic populations, Opt. Lett. **3**, 218 (1978).

[43] Xiaodong Xu, Bo Sun, Paul R. Berman, Duncan G. Steel, Allan S. Bracker, Dan Gammon, and L. J. Sham, Coherent population trapping of an electron spin in a single negatively charged quantum dot, Nat. Phys. **4**, 692 (2008).

[44] Serguei B. Orlinskii, Jan Schmidt, Pavel G. Baranov, Volker Lorrmann, Ingo Riedel, Daniel Rauh, and Vladimir Dyakonov, Identification of shallow Al donors in Al-doped ZnO nanocrystals: EPR and ENDOR spectroscopy, Phys. Rev. B **77**, 115334 (2008).

[45] F. Mohammadbeigi, E. Senthil Kumar, S. Alagha, I. Anderson, and S. P. Watkins, Carbon related donor bound exciton transitions in ZnO nanowires, J. Appl. Phys. **116**, 053516 (2014).

[46] A. V. Rodina, M. Strassburg, M. Dworzak, U. Haboeck, A. Hoffmann, A. Zeuner, H. R. Alves, D. M. Hofmann, and B. K. Meyer, Magneto-optical properties of bound excitons in ZnO, Phys. Rev. B **69**, 125206 (2004).

Correction: The unit given for T_2 in the last sentence of the first paragraph of the Introduction was incorrect and has been fixed. The value given in the sixth row, third column of Table I was incorrect and has been rectified.